Journal of MATERIALS RESEARCH

Article
DOI:10.1557/s43578-021-00367-3

Microstructure in the transition region and steady-state region of ice-templated sintered lithium titanate $Li_4Ti_5O_{12}$ materials fabricated with and without sucrose

Rohan Parai[1], Naga Bharath Gundrati[1], Sashanka Akurati[1], Gary M. Koenig Jr.[2], Dipankar Ghosh[1,a)]

[1] Department of Mechanical and Aerospace Engineering, Old Dominion University, Norfolk, VA 23529, USA
[2] Department of Chemical Engineering, University of Virginia, Charlottesville, VA 22904, USA
[a)] Address all correspondence to this author. e-mail: dghosh@odu.edu

Received: 19 April 2021; accepted: 24 August 2021; published online: 20 September 2021

This study provides insights into the influence of sucrose (a water-soluble additive) on microstructure evolution in the transition region and steady-state region in ice-templated $Li_4Ti_5O_{12}$ materials. A scanning electron microscope was employed for the two-dimensional characterization of microstructure in the transition region. Sucrose reduced the height of the transition region, caused an early alignment of ice lamellae toward temperature gradient direction, and resulted in a fine, dendritic microstructure. The overall microstructure development in the transition region was markedly different with and without sucrose. The differences were rationalized based on thermal conductivity, constitutional supercooling, and instability of the planar interface. Three-dimensional characterization of the steady-state region using X-ray computed tomography revealed that sucrose caused increased branching of the primary ice dendrites through tip splitting. A majority of the secondary dendrites turned into neighboring primary dendrites, enhancing pore path complexity. Diffusion simulations were performed to quantify pore tortuosity, which increased with sucrose content.

Introduction

Ice-templating is a versatile technique that enables the fabrication of novel ceramic materials with directional pore channels [1–5]. The porosity of these materials is a strong function of the solid loading of ceramic suspensions [1, 5–7]. It is of fundamental importance to understand the effects of various intrinsic and extrinsic parameters on microstructure in ice-templated ceramics fabricated from suspensions of the same solid loading. Intrinsic parameters include particle size and shape [3, 8, 9], freezing front velocity (FFV, growth velocity of ice crystals) [3, 6–10], and water-soluble additives [11–15], while extrinsic parameters are energies applied externally during freezing of ceramic suspensions and include magnetic field [16, 17], ultrasound [18, 19] and direct current (DC) electric field [20–22]. Zhao et al. [21] used DC field at high field strength (10–100 kV/m) in the fabrication of ice-templated alumina (Al_2O_3) materials. It was shown that with the increasing field strength, lamella walls were increasingly aligned away from the direction of the applied temperature gradient and spacing of lamella walls increased by more than five times. Zhang et al. [22] prepared dense/porous bi-layered ceramic by applying a DC electric field during freeze casting. Tang et al. [20] applied DC field perpendicular to the direction of the applied temperature gradient. However, both copper (Cu) plates used for the application of DC field also induced freezing. It was observed that with the increasing field strength, lamella walls were increasingly aligned along the field direction and compressive strength also increased in that direction. The use of the magnetic field enables achieving greater control over the alignment of lamella walls and density of lamellar bridges, resulting in enhancement of compressive strength [2, 17]. Ogden et al. [18] implemented ultrasound acoustic waves for the fabrication of ice-templated titania (TiO_2) to mimic the microstructure of naturally occurring materials. The resulting ice-templated TiO_2 materials exhibited structure with porous concentric rings and the number of these rings was controlled by the operating frequency of ultrasound transducer. Overall,

© The Author(s), under exclusive licence to The Materials Research Society 2021

both intrinsic and extrinsic parameters play an important role in both controlling microstructure at different length scales and resulting macroscopic mechanical properties.

In a recent study [23], the authors investigated the role of sucrose (a water-soluble additive) in the fabrication of ice-templated sintered lithium titanate (LTO, composition $Li_4Ti_5O_{12}$) materials, which is an established anode material for lithium (Li)-ion batteries [24, 25]. Materials were fabricated from 20 vol% aqueous LTO suspensions, and the suspensions were prepared without sucrose, as well as with sucrose. In the absence of sucrose, a cationic dispersant was required, whereas LTO suspensions containing sucrose could be prepared without using any dispersant. The addition of sucrose up to 4 wt% (with respect to water content in suspension) caused only a marginal reduction in porosity in sintered materials. However, with the increasing sucrose content, lamellar bridge density increased significantly, morphology changed from lamellar (without sucrose) to dendritic (with sucrose), and uniaxial compressive strength enhanced remarkably [23]. However, for an improved understanding of the role of sucrose on structure–property relationships, in-depth characterization of the microstructure of these materials is needed, which was lacking in the previous study.

The ice-templated microstructure is a negative replica of the morphology of the removed ice crystals. At the beginning of freezing, ice crystals grow rapidly, and particles in the suspension are engulfed by a planar growth front [26–28]. As the growth velocity decreases, the planar interface between ice crystals and suspension experiences instability, and lamellar/dendritic crystals develop, which grow steadily in the direction of the applied temperature gradient until the completion of solidification [26–29]. A transition region thus exists, where ice crystals undergo morphological changes, and by the end of this zone, ice lamellae achieve a preferred alignment toward the temperature gradient direction. In the steady-state region, lamellar/dendritic ice crystals continue to grow with particles accumulating between the crystals, and the characteristic ice-templated lamellar/dendritic morphology develops. The morphological changes in the transition zone directly influence the templated microstructure in the steady-state region.

Therefore, in-depth knowledge of microstructure both in transition and steady-state regions and the influence of variables on the microstructure of these regions are of utmost importance toward the development of ice-templated materials with targeted properties. In the majority of the studies, however, little emphasis is given on the transition zone microstructure. The aim of this study is to thoroughly characterize the microstructure of both transition and steady-state regions in ice-templated sintered LTO materials fabricated without and with sucrose. Significant insights into the role of sucrose on morphology, orientation, and growth characteristics of ice crystals in both regions were provided from in-depth microstructure characterization of sintered materials, which presents a negative replica of the removed ice crystals.

A scanning electron microscope (SEM) was employed to characterize microstructural differences in the transition region. By performing X-ray computed tomography (XCT) using a three-dimensional (3D) X-ray microscope (XRM), microstructure for significant depth ranges in the growth direction for the steady-state region was characterized. XCT is a well-suited visualization tool for the 3D characterization of complex, heterogeneous microstructure in porous solids [30, 31]. From XCT data, the tortuosity factor related to diffusive properties [32–34] was estimated by performing mass transport simulations using a TauFactor application in MATLAB [35–37]. In-depth knowledge of the influence of water-soluble additives on microstructure evolution both in the transition region and steady-state region in ice-templated LTO materials will have significant implications on rational control of mechanical properties, pore tortuosity, and microstructure transport properties. Such microstructure transport is important for the development of these materials for Li-ion batteries [23, 38].

Results and discussion

Microstructure in transition region

Microstructure evolution: image plane parallel to growth direction

The SEM images in Fig. 1 show vertical cross-section (x–z plane) parallel to the z-direction, revealing microstructure in the transition region across the three compositions, LTO-0, LTO-1, and LTO-4. Orange dotted lines in Fig. 1c indicate the heights of x–y planes along z-direction from where SEM images were obtained for all the materials, shown in Figs. 2 and 3. In Fig. 1a–c, two zones (I and II) are identified, and dotted orange lines do not indicate the boundaries between these zones. Zone I is the very bottom region, a relatively dense region of thickness about 100 μm (higher magnification images are shown in d–f). Also, SEM images of the bottommost x–y plane are shown in Supplementary Fig. S1. At the beginning of freezing, the ice crystals grow rapidly, and particles are engulfed within the crystals [26–28]. As a result, a relatively dense region develops in sintered materials. Figure 1g–l shows higher magnification images of zone II. Images in g–i represent the region close to zone I, and images in j–l represent the region above the region shown in g–i. Zone II is a region between the bottommost dense layer and the region where the characteristic templated structure has fully developed. For LTO-0, most of the region shown in Fig. 1g contains randomly oriented pores; however, lamella walls developed in the upper region but are almost perpendicular to z-direction.

© The Author(s), under exclusive licence to The Materials Research Society 2021

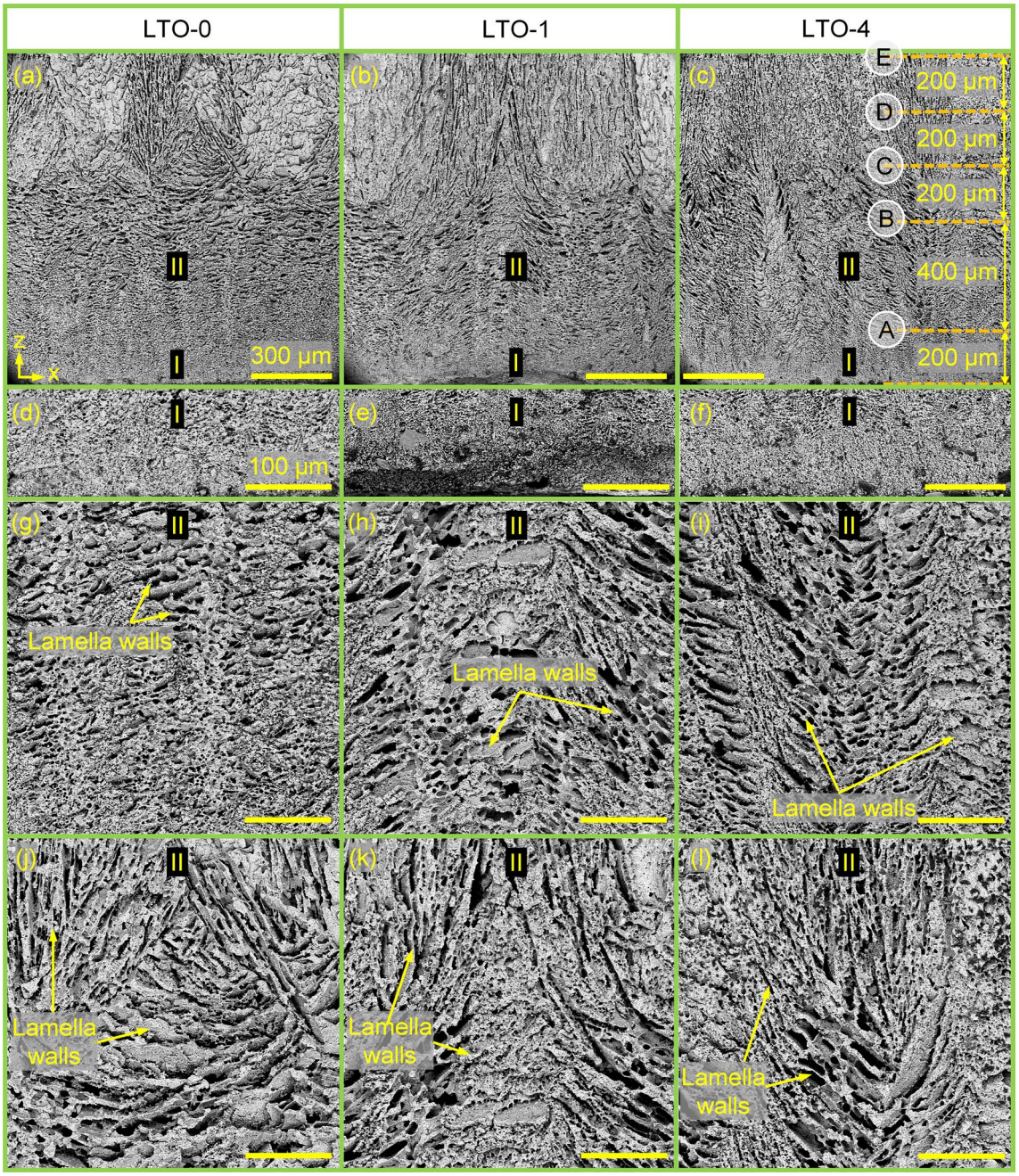

Figure 1: Representative SEM images of *x*–*z* plane revealing the transition region in LTO-0 (a), LTO-1 (b), and LTO-4 (**c**). Orange dotted lines in (c) indicate the heights of *x*–*y* planes along *z*-direction from where SEM images were obtained for all the materials, shown in Fig. 2 (LTO-0) and Fig. 3 (LTO-1, LTO-4). Higher magnification SEM images of zone I and zone II are shown in (d–f) and (g–l), respectively. Scale bar in (a–c) 300 μm and (d–l) 100 μm.

In LTO-1 and LTO-4, lamella walls are observed throughout the images in Fig. 1h and i and inclined toward *z*-direction. Figure 1j–l reveals lamella walls in all the materials; however, a greater fraction of walls is oriented toward *z*-direction in LTO-1 and LTO-4 than in LTO-0.

Microstructure evolution: image plane perpendicular to growth direction

SEM images of *x*–*y* planes at different heights along *z*-direction for LTO-0 are shown in Fig. 2 and for LTO-1 and LTO-4 in

© The Author(s), under exclusive licence to The Materials Research Society 2021

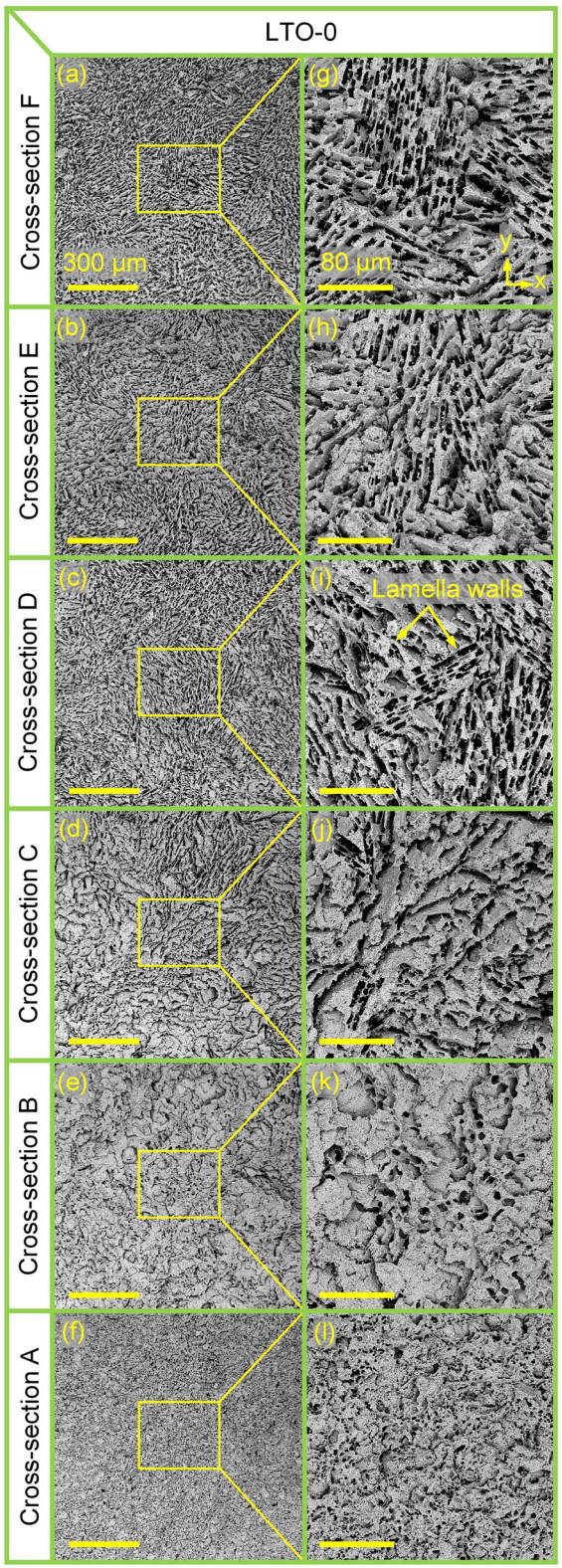

Figure 2: Representative low-magnification (a–f) and high-magnification SEM images (g–l) of LTO-0, revealing microstructure evolution in the transition region on *x*–*y* plane at different heights along *z*-direction. Scale bar in (a–f) 300 μm and (g–l) 80 μm.

Fig. 3. Image plane F (not shown in Fig. 1c) is located 200 μm above image plane E. For each material, low- and high-magnification images are shown in the left column and right column, respectively. Additional higher magnification SEM images are shown in Supplementary Figs. S2, S3 and S4.

At location A of LTO-0, the microstructure contains randomly oriented pores (cellular pores); also see Supplementary Fig. S2a. At location B, ceramic lamella walls have started to develop but are oriented randomly on the *x*–*y* plane and almost perpendicular to *z*-direction. At location C, the development of walls is more prominent with some preferred alignment of the walls toward *z*-direction; also see Supplementary Fig. S2b. At location D, a greater fraction of the walls is aligned toward *z*-direction. With increasing height, ice-templated microstructure continued to develop with the increasing alignment of walls. However, even at location F, the ice-templated microstructure was not fully developed. Further microstructure investigation revealed that at about 2 mm height, all the walls were approximately aligned along the *z*-direction, suggesting the end of the transition zone.

During ice-templating, in zone II, as the growth velocity starts to diminish, breakdown of the solid–liquid planar interface (developed in zone I) occurs, and particle rejection by ice crystals begins [26]. In zone II of LTO-0, ice crystals with cellular morphology developed and grew with random orientations relative to the *z*-direction. With the upward advancement of the growth front, ice lamellae developed but were oriented randomly on the *x*–*y* plane. The rejected LTO particles accumulated between the ice lamellae, resulting in ceramic walls. With the continued upward movement of the growth front, ice lamellae began to align toward *z*-direction preferentially. Thus, in the transition region, the growth front gradually changed from planar to cellular to lamellar morphology. Such interface transition is attributed to the Mullins–Sekerka (MS)-type instability mechanism, which results from constitutional supercooling [39]. During solidification under constrained growth conditions, the MS-type instability causes the breakdown of the solid–liquid planar interface to cellular morphology, which next transforms to lamellar/dendritic morphology. The lamellar shape of ice crystals results from the strong growth anisotropy of hexagonal ice crystals. In hexagonal ice, growth along the *c*-axis is theoretically two orders of magnitude slower than growth along the *a*-axis and *b*-axis, resulting in the lamellar shape of ice crystals [27].

From the XCT images of unidirectionally frozen aqueous Al_2O_3 suspension, Deville et al. [27] identified two populations of lamellar ice crystals in the transition zone: ice lamellae oriented toward temperature gradient (z-crystals) and perpendicular to the gradient (r-crystals). The morphology of both crystals

© The Author(s), under exclusive licence to The Materials Research Society 2021

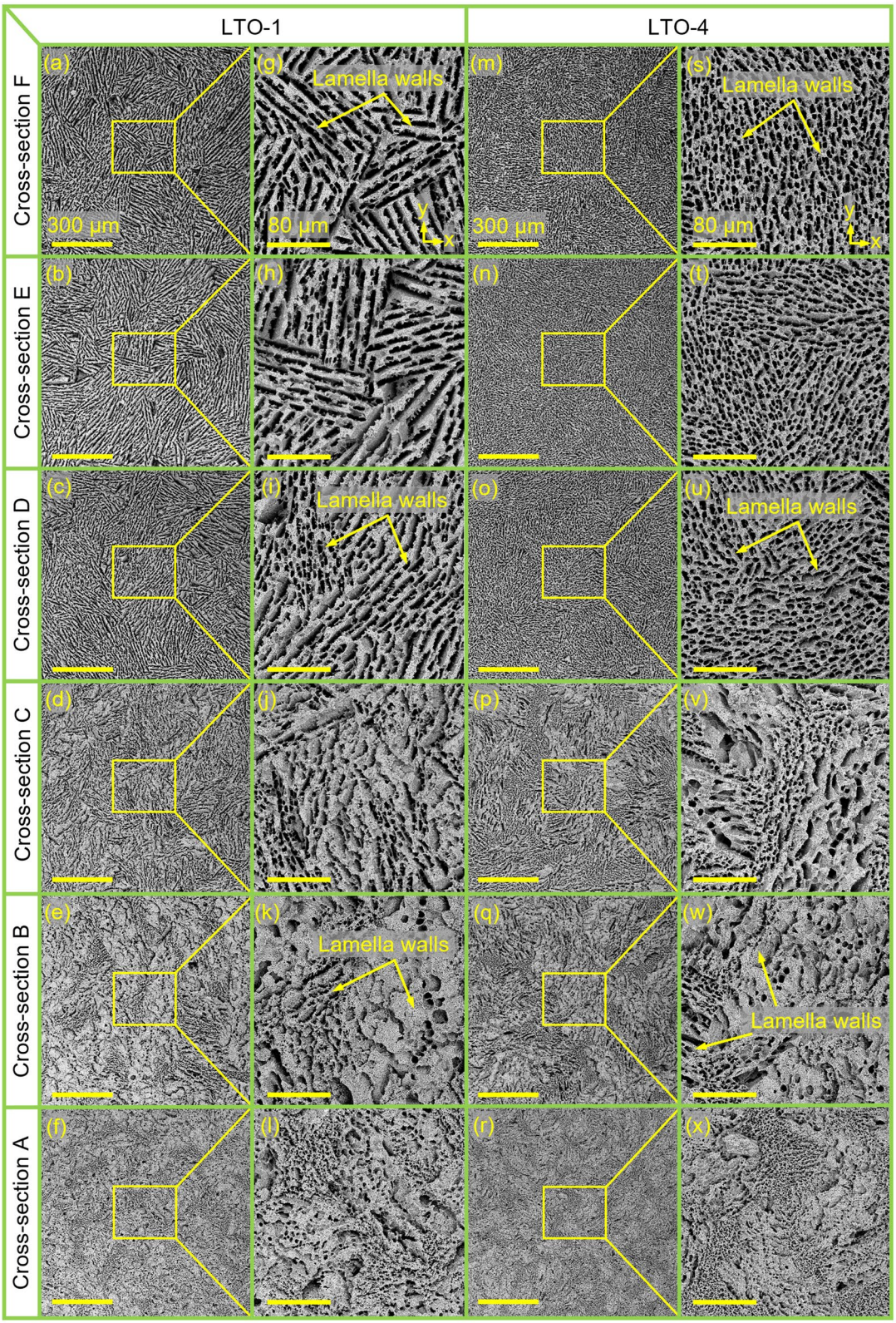

Figure 3: Representative low-magnification (a–f) and high-magnification SEM images (g–l) of LTO-1, revealing microstructure evolution in the transition region on *x*–*y* image plane at different heights along *z*-direction. Similarly, low-magnification (m–r) and high-magnification (s–x) SEM images of LTO-4, revealing microstructure evolution in the transition region on *x*–*y* image plane at different heights along *z*-direction. Scale bar in (a–f) 300 μm, (g–l) 80 μm, (m–r) 300 μm, (s–x) 80 μm.

© The Author(s), under exclusive licence to The Materials Research Society 2021

is the same but referred to as z- and r-crystals because of their orientation difference relative to the applied temperature gradient direction. With the upward movement of the freezing front, the population of z- and r-crystals increased and decreased, respectively, with all r-crystals disappeared by the end of the transition zone. In LTO-0, even at 600 μm height from the bottom (740 μm height in the frozen sample, considering 23% linear shrinkage due to sintering), ceramic walls were mostly oriented on the *x*–*y* plane (Fig. 2k), and hence the ice lamellae (r-crystals) in the frozen sample. Thus, the population of r-crystals dominated up to a significant height in the transition region. Since the formation of lamella walls oriented toward *z*-direction is observed at 800 μm from the bottom, by this height, a small fraction of r-crystals turned into z-crystals. With the upward movement, as the growth velocity slows down, the temperature gradient provides a strong driving force for the alignment of ice lamellae toward the gradient, i.e., promotes the growth of z-crystals. Gradual alignment of ceramic walls toward the thermal gradient suggests progressive extinction of r-crystals and preferential growth of z-crystals, and the r-crystals completely disappeared by the end of the transition region [27].

Deville et al. [27] proposed that the extinction of r-crystals and preferential growth of z-crystals are associated with the thermal conductivity of the domains containing these crystals. A domain is referred to as a region that contains one type of ice crystal (r or z) with accumulated ceramic particles between ice lamellae. Figure 4a schematically shows the arrangement of r-crystal and z-crystal domains with respect to the direction of the applied temperature gradient. For each domain type, only one layer of ice crystal and one layer of particle phase are shown. Relative to the *z*-direction, the thermal resistance of the particle-rich phase and ice act in series in the r-crystal domain, but they

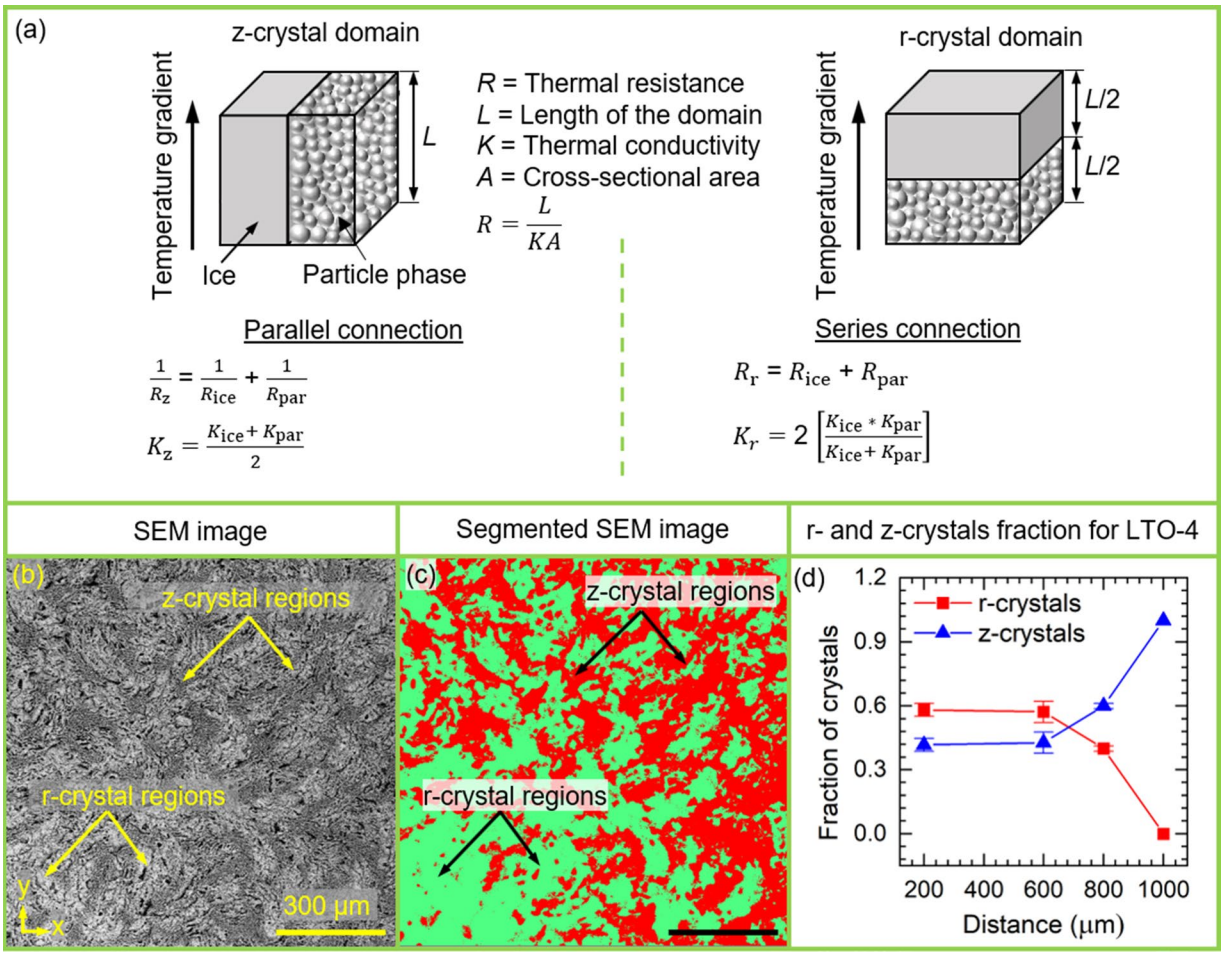

Figure 4: (a) Schematics show the arrangement of r-crystal and z-crystal domains with respect to the direction of applied temperature gradient, overall growth direction (*z*-direction). For each domain type, only one layer of ice crystal and one layer of particle phase are shown. Relative to the *z*-direction, thermal resistance of the particle-rich phase and ice act in series in r-crystal domain but they are in parallel connection in z-crystal domain. In (a), also shown are the equations for thermal resistance (R) and conductivity (K). Equations for K of z-crystal (K_z) and r-crystal domains (K_r) are expressed in terms of the individual thermal conductivities of ice (K_{ice}) and particle phase (K_{par}) and domain dimensions. (b) Representative SEM image of *x*–*y* plane at location A in LTO-4. (c) Segmented SEM image. (d) Variation in area fractions of r-crystals and z-crystals with distance along the *z*-direction in the transition region.

© The Author(s), under exclusive licence to The Materials Research Society 2021

are in parallel connection in the z-crystal domain. Figure 4a also shows the equations for thermal conductivity of z-crystal (K_z) and r-crystal domains (K_r), expressed in terms of the individual thermal conductivities of ice (K_{ice}) and particle phase (K_{par}) and domain dimensions. Details of the derivations can be found in Supplementary Materials. Thus, the thermal conductivity of a crystal domain depends mainly on the thermal conductivity of the individual layers and the arrangement of the layers (series or parallel). K_{ice} of ice is low, ranging between 1.6 and 2.4 W/mK [27]. If K_{par} is considerably greater than K_{ice}, K_z is mainly dependent on K_{par}, whereas K_r on K_{ice}. Therefore, for higher K_{par}, K_z will be higher than K_r, making z-crystal domains effective paths for heat transfer along the *z*-direction. As a result, higher K_{par} will promote the growth of z-crystals at the expense of r-crystals. On the other hand, for comparable K_{ice} and K_{par}, the thermal conductivity of both crystal domains will be similar, which would retard the preferential growth of z-crystals. Since the thermal conductivity of LTO (~2.5 W/mK at 500 K) is close to that of ice [40], it is possible that in LTO-0, the preferential growth of z-crystals was retarded, and the r-crystal population dominated up to a significant height in the transition region.

From Fig. 3, it is evident that in LTO-1 and LTO-4, lamella walls developed at the earlier stages of growth. By location E (1.2 mm from bottom), characteristic ice-templated microstructure has fully developed, indicating the end of the transition zone and shorter length of this zone than in LTO-0. At lower heights, low-magnification SEM images (Fig. 3f, r, location A) show a significant contrast difference between the neighboring regions. Higher magnification images (Fig. 3l, x) suggest that the relatively darker regions contain fine pores with thin walls, whereas the relatively lighter regions contain larger pores with relatively thick walls; also see Supplementary Fig. S3a. Pores appear to be of cellular morphology in both the regions. With the upward movement of the growth front, lamella walls developed in both regions. However, a remarkable difference in wall thickness can be seen between the regions; see Supplementary Fig. S3b for LTO-4 at location B. Moving further upward, the area fraction of the regions containing fine pores increased, the formation of walls becomes more prominent with an increase in the alignment toward *z*-direction, particularly in the regions with fine pores, and thickness of walls in the regions surrounding the fine pores increased greatly; see Fig. 3p, v and Supplementary Fig. S3c for LTO-4 at location C. By location D, the contrast difference between the neighboring regions diminished, the regions with thick ceramic walls and large pores disappeared, and dendritic morphology (enhanced bridging between walls) with thin lamella walls and small pores developed in LTO-4 (higher magnification images are shown in Supplementary Fig. S4). Microstructures at locations E and F appear similar to those at location D. A similar transition of microstructure also occurred in LTO-1; however, the morphology (at D, E, F) appears considerably less dendritic than LTO-4. Overall, Fig. 3 suggests that along the *z*-direction, the area fraction of the regions containing fine pores increased, and cellular pores in these regions transformed into the characteristic directional pores. Also, at the early stages of growth, lamella walls achieved a more preferred alignment toward *z*-direction compared to that in LTO-0.

The above analysis suggests that sucrose strongly influenced the morphology, orientation, and growth characteristics of ice crystals in the transition region. In LTO-1 and LTO-4, the morphology of ice crystals transitioned from planar to cellular to lamellar (LTO-1) or to highly dendritic (LTO-4) morphology; thus, MS-type instability also occurred in these materials. In the presence of sucrose, homogeneously distributed regions with both fine and coarse cellular ice crystals evolved. While in ice-templating, cellular ice crystals develop at the early stages of solidification, sucrose reduced the size of these crystals, and the volume fraction of fine ice crystals increased with sucrose content. With the upward movement of the growth front, ice lamellae developed in both regions. However, coarse ice lamellae were progressively replaced by fine ice lamellae, which achieved preferred alignment toward *z*-direction at the early stages of growth.

Therefore, a striking difference between the materials fabricated without and with sucrose is observed in the evolution of z-crystals in the transition region. As discussed before, during ice-templating of LTO-0, r-crystals first developed, which gradually transformed to z-crystals. In LTO-1 and LTO-4, on the other hand, fine cellular ice crystals were directly transformed into z-crystals. It is possible that in these materials, r-crystals developed in the regions containing coarse cellular ice crystals (brighter regions), whereas z-crystals evolved in the regions containing fine cellular ice crystals (lighter regions). This is interpreted based on the similarity of the microstructure in the regions containing large cellular pores in LTO-4 and the microstructure of LTO-0 (Fig. 2k). Note that the fraction of the regions with larger cellular pores is higher in LTO-1 than in LTO-4, and the microstructure of LTO-1 is between that of LTO-0 and LTO-4. Thus, as ice crystals transitioned from cellular to lamellar/dendritic morphology, both crystal types likely existed at the very early stages of growth as opposed to LTO-0, where the r-crystal population dominated up to a greater height in the transition region. The early development of z-crystals also resulted in the early termination of the transition region in LTO-1 and LTO-4.

Finally, Fig. 4b–d compares the variation of area fractions of regions containing fine pores (darker regions in SEM images, presumably were occupied by z-crystals) and coarse pores (brighter regions in SEM images, presumably were occupied by r-crystals) with distance along the *z*-direction in LTO-4. Using the open-source image processing software Fiji: ImageJ® (NIH,

© The Author(s), under exclusive licence to The Materials Research Society 2021

USA), area fractions were estimated from SEM images of x–y plane. For each cross-sectional plane, five SEM images were used. Figure 4b shows a representative SEM image for LTO-4 at location A. SEM images were segmented into two-phase regions using "Trainable Weka Segmentation (TWS)" plugin, which performs image-segmentation by categorizing the regions in the image based on the visual characteristics of the pixels. A segmented SEM image is shown in Fig. 4c, where brighter and darker regions are identified in green and red colors, respectively. Figure 4d shows the variation of area fractions of r-crystals and z-crystals with distance along the z-direction. Initially, the area fraction of r-crystals is observed to be considerably higher than that of z-crystals and change in area fraction is minimal up to a distance 600 μm (location B) in the transition region. However, beyond that, area fractions of these regions changed markedly, with r-crystals disappearing completely by a distance 1000 μm from bottom (location D).

Interface instability in transition region and effects of sucrose

As mentioned earlier, the MS-type interface instability during solidification under constrained growth conditions originates from constitutional supercooling, which is mainly caused by solute accumulation ahead of solid–liquid planar interface [27, 39, 41–45]. Constitutional supercooling and interface instability play an important role in microstructure evolution in ice-templated materials [2, 4, 27, 42]. Greater constitutional supercooling could be responsible for the differences observed in microstructure in the ice-templated LTO materials fabricated with and without sucrose. During the beginning phase of unidirectional freezing of aqueous colloidal suspensions, the solid–liquid interface grows as a planar interface. Due to the low solubility of solute in solid than in liquid, solute molecules (such as dispersant and binder molecules) are rejected by growing ice crystals and pile up ahead of planar interface [40]. As a result, a boundary layer of solute develops in front of planar interface, in which solute concentration reaches maximum C_o/k at the interface but decreases away from the interface to bulk solute suspension concentration C_o, which defines the end of the boundary layer. This limiting solute concentration at the interface is often assumed to be the eutectic composition [46]. Distribution coefficient k (<1) describes solute compositional difference between liquid phase and solid phase [41, 42]. The exponential decrease of solute concentration in liquid phase (C_l) with distance (x) from interface in the boundary layer is expressed as [41, 42]:

$$C_l = C_o + (C_o/k - C_o)\exp(-vx/D). \quad (1)$$

v is interface velocity and D is solute diffusion coefficient in liquid. Due to the increased solute concentration in the suspension at the interface, the net result is a decrease of the local equilibrium solidification temperature in the liquid (liquidus temperature, T_{liq}) at the interface (i.e., freezing point depression) compared to bulk T_{liq}. However, the local T_{liq} increases away from the interface and reaches bulk T_{liq} at the end of the boundary layer. The thickness of the boundary layer (δ) can be estimated as [42]:

$$\delta = 2D/v. \quad (2)$$

The above equations suggest that increase in v will cause a decrease of C_l in the boundary layer and reduce δ. Increase in interface growth velocity will result in a steeper boundary layer because of a higher rate of solute rejection but there will be less time available for the rejected solute molecules to diffuse away from the interface. Therefore, with the increasing v, C_l from interface will drop sharply, and as a result, δ will also decrease [42]. Similar effects will result from the decrease of D as well, which is directly associated with suspension viscosity. An increase in suspension viscosity will result in a decrease of the diffusivity of solute molecules in the suspension.

Interface velocity strongly depends on applied temperature gradient [42]. In the current study, all LTO suspensions were subjected to a similar gradient and the measured average interface growth velocity was highly comparable across the three compositions. The average FFV values are provided in "Fabrication of ice-templated sintered LTO materials" section. On the other hand, the variation in D of solutes between the suspensions without and with sucrose could have affected both C_l and δ. To this end, Fig. 5a shows the variation of viscosity of LTO suspensions with shear rate. Among the three compositions, at shear rate of 0.1 s^{-1}, LTO-1 exhibited the lowest viscosity, whereas LTO-4 exhibited much higher viscosity compared to the other suspensions. Recall that the only composition difference among the suspensions is that LTO-0 contained CTAB dispersant, whereas LTO-1 and LTO-4 contained sucrose. In LTO-0, CTAB concentration was 0.05 mol/L. For LTO-1 and LTO-4, sucrose concentration was 0.03 mol/L and 0.12 mol/L, respectively. Therefore, solute concentration increased from LTO-1 to LTO-0 to LTO-4. Binder concentration was same in all the suspensions, 0.35 mol/L. Therefore, the excess amount of sucrose in LTO-4 suspension caused a significant increase in viscosity compared to the other LTO suspensions. Between LTO-4 and LTO-0, it is expected that higher suspension viscosity in LTO-4 resulted in lower D of solute molecules compared to that in LTO-0. As a result, solute molecules in LTO-4 suspension (sucrose and binder molecules) rejected at the planar interface experienced greater resistance to diffuse away from the interface than in LTO-0 suspension (CTAB and binder molecules). Therefore, solute boundary layer is expected to be thinner with a steeper concentration profile of solute molecules in LTO-4 than in LTO-0. The differences in solute boundary layer likely influenced the degree of constitutional supercooling [47, 48].

However, before embarking further on constitutional supercooling, Fig. 5b shows the variation of wavelength (λ, indicated

© The Author(s), under exclusive licence to The Materials Research Society 2021

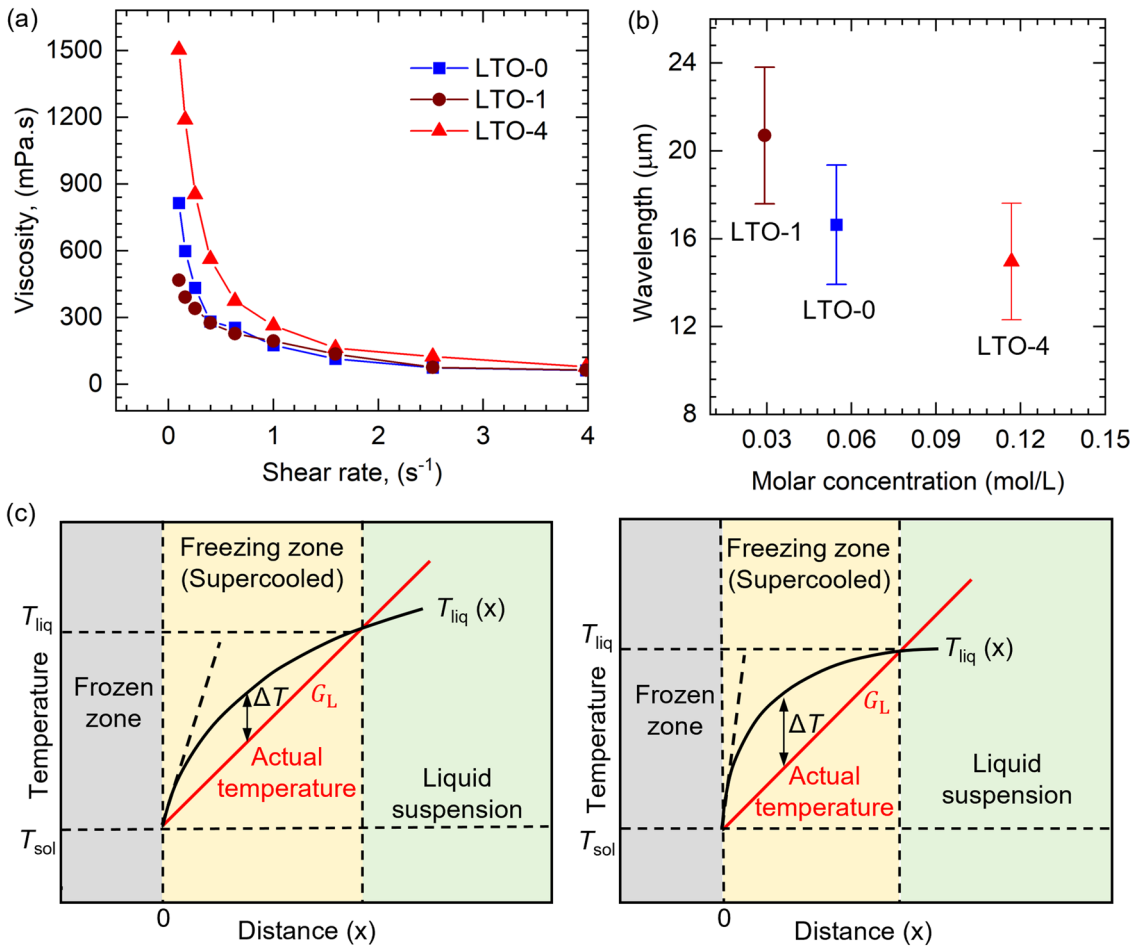

Figure 5: (a) Variation of viscosity with shear rate for LTO-0, LTO-1, and LTO-4 suspensions. (b) Variation in wavelength in sintered LTO-0, LTO-1, and LTO-4 materials with respect to the molar concentration in respective suspensions. (c) Schematics show the variation of liquidus temperature (T_{liq}) with distance (x) from solid–liquid planar interface for LTO-0 and LTO-4 suspensions subjected to same temperature gradient G_L. Shaded regions shown are frozen zone, freezing zone, and suspension (liquid). The actual suspension temperature in the freezing zone at a distance x from the interface is determined by G_L, whereas $T_{liq}(x)$ represents equilibrium solidification temperature of the liquid at x.

in Fig. 6a), measured from image plane perpendicular to the growth direction and at a height of 2 mm from bottom, with solute concentration in LTO suspensions, CTAB concentration for LTO-0 and sucrose concentration for LTO-1 and LTO-4. λ Represents spacing between primary ice dendrites (discussed in "Microstructure in steady-state region" section). With the increasing solute concentration (from LTO-1 to LTO-0 to LTO-4), a consistent decrease in λ is observed. For ice-templated ceramics, the decrease in λ with the increasing additive concentration and/or viscosity has been reported [4, 49]. The decrease in λ is also inversely related to the degree of constitutional supercooling (ΔT). According to Porter et al. [4], ΔT is related to λ as:

$$\Delta T \sim A/\lambda. \tag{3}$$

Thus, with the increasing viscosity of LTO suspension, the decrease of λ suggests an increase of ΔT, i.e., greater interface instability during directional solidification.

Returning to constitutional supercooling, Fig. 5c schematically shows the variation of T_{liq} with distance from solid–liquid planar interface for LTO-0 and LTO-4 suspensions subjected to the same temperature gradient G_L. In the temperature–distance diagram, the shaded regions represent frozen zone (completely solid, containing ice crystals and particles), freezing zone (containing ice, particles, and liquid), and suspension (liquid). The actual suspension temperature in the freezing zone at a distance x from the interface is determined by G_L, whereas $T_{liq}(x)$ represents the equilibrium solidification temperature of the liquid at x [41–43]. T_{liq} is depressed at the interface but increases away from the interface and reaches bulk T_{liq}. When the applied temperature gradient is lower than the gradient in the liquidus temperature curve (indicated by dashed black line on each curve), a supercooled region develops ahead of the planar interface where liquid exists below the freezing temperature, which is referred to as constitutional supercooling, or more specifically, solute

© The Author(s), under exclusive licence to The Materials Research Society 2021

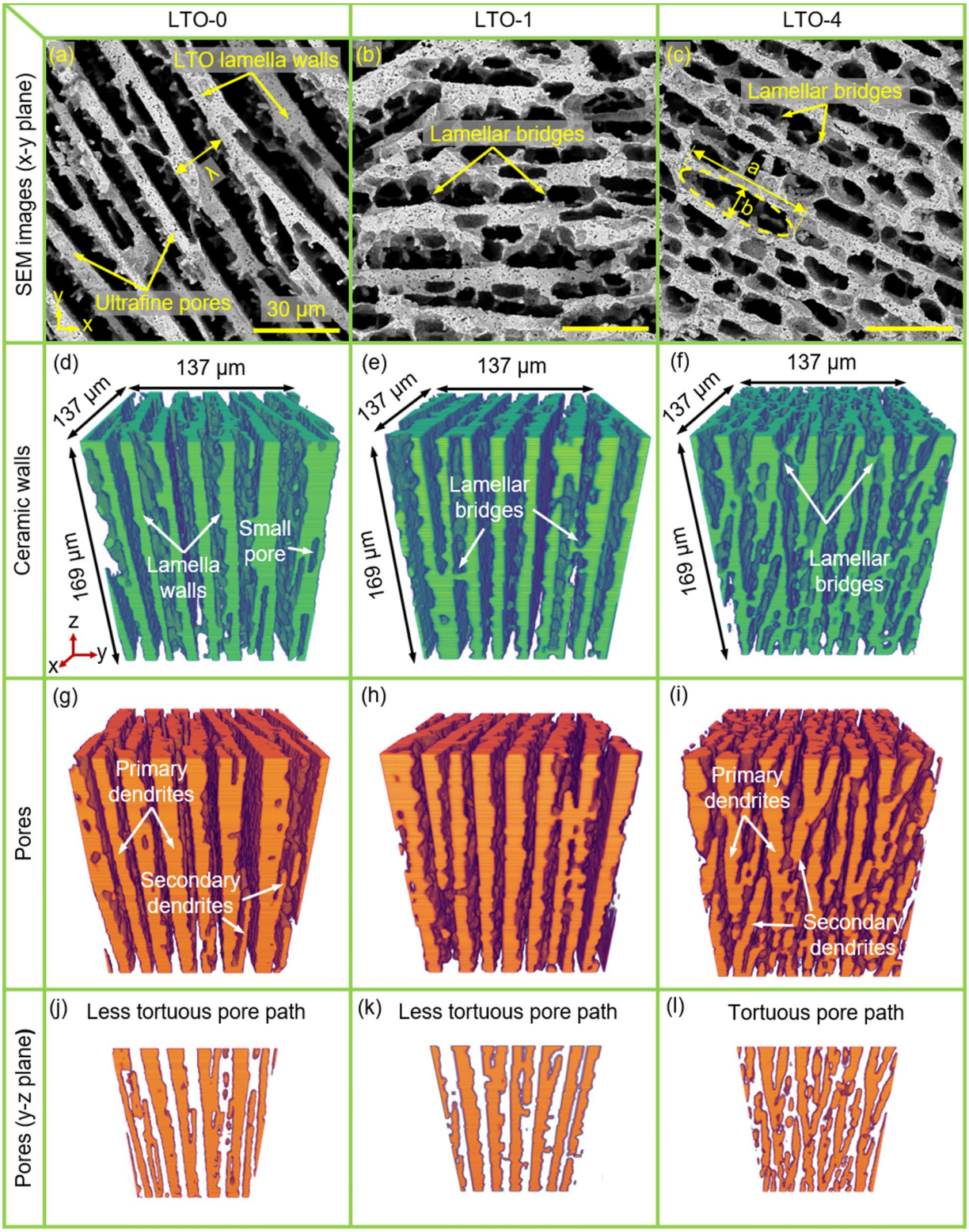

Figure 6: Representative SEM images of *x*–*y* plane for LTO-0 (a), LTO-1 (b), and LTO-4 (c), revealing microstructure in the steady-state region. Scale bar in (a–c) 30 μm. (d–f) XCT 3D volume renderings (137 μm × 137 μm × 169 μm), in which colored regions (green) represent ceramic walls and empty regions represent pores. (g–i) XCT 3D volume renderings (137 μm × 137 μm × 169 μm), in which colored regions (orange) are pores and empty regions are walls. (j–l) 2D images of pore channels on the *y*–*z* plane, revealing increased complexity and tortuosity of the pore path along the growth direction due to sucrose.

© The Author(s), under exclusive licence to The Materials Research Society 2021

constitutional supercooling [45]. In Fig. 5c, ΔT represents the maximum degree of supercooling. The liquid in the supercooled region is in a metastable condition, which provides a driving force for the perturbation of the solid/liquid planar interface, i.e., interface instability [42].

In Fig. 5c, it is shown that ΔT is greater in LTO-4 than in LTO-0. Solute phase (dispersant, binder) is known to depresses T_{liq} of suspensions [41, 42, 50], which suggests lower bulk T_{liq} in LTO-4 than in LTO-0. However, without the measurements, which is beyond the scope of this work, it is challenging to predict the variation of T_{liq} across the LTO suspensions of different compositions. However, it has been discussed above that solute boundary layer is thinner and steeper in LTO-4 than in LTO-0. As a result, as depicted in Fig. 5c, T_{liq} in LTO-4 quickly increases away from the interface and reaches bulk liquidus temperature, whereas T_{liq} in LTO-0 gradually increases away from the interface and reaches bulk liquidus temperature. It has been reported by Harrison and Tiller [47] that steeper solute concentration profile leads to a greater degree of constitutional supercooling. Therefore, it is suggested that the variation in the change of T_{liq} with distance from interface due to different solute concentration profiles also resulted in the difference of ΔT between LTO-0 and LTO-4 suspensions, causing greater interface instability in LTO-4. For the same applied G_L, ΔT is thus expected to be higher for the suspension with higher viscosity. Based on the above discussion, it is interpreted that during directional freezing, LTO-4 suspension was in a higher state of metastable condition than LTO-0 suspension. It is known that the greater the interface instability, the higher is the driving force for breakdown of planar interface [42]. Therefore, compared to LTO-0 suspension, LTO-4 suspension experienced a greater driving force for breakdown of planar interface. One prominent effect of greater interface instability is the formation of large number of fine, dendritic ice crystals in the transition region of LTO-4 [51]. As a result, LTO-4 exhibited considerably finer microstructure than LTO-0.

Microstructure in steady-state region

Figure 6a–c shows SEM images of LTO-0, LTO-1, and LTO-4 materials, where each image corresponds to x–y plane in the steady-state region, at the height of 2 mm from the bottom. Lamella walls in all the materials contain a considerable amount of micropores. With the increasing concentration of sucrose, the density of lamellar bridges significantly increased, and as a result, pore size decreased, particularly pore major axis, a. Thus, major microstructure differences across the compositions are also observed in the steady-state region. A dimensionless morphological parameter "m" was estimated for the LTO materials, which is defined as [52]:

$$m = \frac{(1/\rho_b)}{\lambda^2}, \tag{4}$$

where ρ_b is lamellar bridge density, and λ is the wavelength (indicated in Fig. 6a). λ is defined as the sum of lamella wall thickness and pore minor axis (b, indicated in Fig. 6c). In Eq. (4), $1/\rho_b$ represents the square of the spacing of the bridges, which is divided by the square of the wavelength of lamella walls. Naglieri et al. [52] suggested that pore morphology is lamellar for $m > 5$, dendritic for $1 < m < 5$, and isotropic for $m < 1$. The estimated m values for LTO-0, LTO-1, and LTO-4 were about 15, 6, and 3, respectively. The morphology of LTO-0 is highly lamellar but turned into dendritic in LTO-4 due to increased bridge density. Thus, the morphology developed in the transition region was also maintained in the steady-state region.

For each material, the tomography dataset corresponds to volume 540 µm × 540 µm × 790 µm with 790 µm is height along the growth direction. Each XCT 3D image was reconstructed from 987 2D images. These images are shown in Supplementary Fig. S5. However, to provide better insights, here, 3D renderings of smaller volume are shown. Figure 6d–f shows XCT 3D renderings (137 µm × 137 µm × 169 µm), in which colored regions represent ceramic walls and empty regions represent pores. Similarly, Fig. 6g–i shows 3D volume renderings (137 µm × 137 µm × 169 µm), in which colored regions are pores and empty regions are walls. All the pores were initially occupied by ice crystals developed during the templating process. Although sintering causes shrinkage, overall pore morphology (thus also the morphology of ice crystals removed through freeze-drying) is nevertheless mostly preserved. Therefore, Fig. 6g–i provides a 3D view of ice crystals, enabling an improved understanding of the role of sucrose on ice crystal morphology. Finally, Fig. 6j–l shows 2D images of pore channels on the y–z plane, revealing the increased complexity and tortuosity of the pore path along the growth direction due to sucrose. In these images, ultrafine pores (< 1 µm) within LTO walls could not be observed due to the resolution limit, since here voxel edge length is 800 nm and resolution is known to be about three times of voxel edge length [40]. 3D images of several regions along the growth direction (z-direction) of ice crystals for all the materials are shown in Supplementary Fig. S6, which indicate minimal microstructure variation along the growth direction within the height of 790 µm.

LTO-0 exhibits relatively straight ceramic walls and pore channels, continuous along the growth direction (z-direction). There is limited interlamellar connectivity, hence lamellar morphology. In the frozen state, large pore channels were occupied by primary ice dendrites. Small, local pores protruding out of primary pore channels were occupied by secondary ice dendrites, which did not extend to the adjacent primary ice dendrite. The formation of a secondary dendrite is associated with the tip splitting (side brunch instability) of a primary dendrite, often referred to as twin dendrites [29]. Typically, secondary dendrites emerging due to side branch instabilities do not evolve

© The Author(s), under exclusive licence to The Materials Research Society 2021

into primary dendrites because by the time such protruding dendrites could turn into stable dendrites growing along the z-axis, surrounding crystals have already grown [29]. Due to limited space for growth as primary dendrites, these secondary dendrites either terminate between the primary crystals or grow to reach the adjacent primary crystal [29]. Figure 6g, j clearly suggests limited tip splitting of primary ice dendrites and growth of secondary ice dendrites in LTO-0, which are characteristic features in ice-templated materials fabricated from low solid loading suspensions.

In the steady-state region, the microstructure of LTO-0 and LTO-1 is observed to be similar. On the other hand, microstructural complexity increased significantly with 4 wt% sucrose content. In LTO-4, along the z-direction, side branching of lamella walls markedly increased and hence interlamellar connectivity, attributing to reduced pore size. The increased branching of ceramic walls also significantly reduced the straightness of walls along the growth direction. The increased branching of lamella walls is directly related to the increased branching of primary ice dendrites, which experienced greatly enhanced tip splitting. A majority of the secondary dendrites grew into neighboring primary dendrites. The primary dendrites that emerged from secondary dendrites again underwent tip splitting and generated secondary dendrites, and the process continued. XCT 3D images suggest that while pore continuity along the growth direction is still maintained in LTO-4, pore path tortuosity increased due to sucrose.

Figure 7 compares the orientation distribution of lamella walls for LTO-0, LTO-1, and LTO-4 with respect to the z-direction, determined from binarized 2D XCT images of y–z plane. For this purpose, the "Directionality" plugin (Directionality: ImageJ) in Fiji-ImageJ® was used. Figure 7a, b, and c shows representative binarized XCT 2D images (250 μm × 700 μm) of LTO-0, LTO-1, and LTO-4, respectively. For each material, five images were used to estimate the distribution of lamella wall orientation, and the results are presented in Fig. 7d. For LTO-0 and LTO-1, orientation distributions are observed to be narrow and comparable. Misalignment of lamella walls is expected since, in ice-templated ceramics, not all the lamella walls develop precisely parallel to the direction of an applied temperature gradient, and the walls are also not parallel to each other [7, 53, 54]. Both LTO-0 and LTO-1 also show a narrow distribution of orientations of lamella walls. On the other hand, for LTO-4, the distribution of lamella walls is broad, with a significant shift in θ, attributed to significant branching in walls.

For more insights into the pore path characteristics and differences, Fig. 8 shows 3D images of a few pore channels in LTO-0 (a) and LTO-4 (b) over a distance of 400 μm. The front y–z plane is colored in yellow for better visualization, and the colored regions (yellow and orange) represent pores. The y–z plane is moved backward along the x-direction to provide more insights into pore path characteristics. In LTO-0, two individual pore channels (#1 and #2) are continuous along the z-direction. A similar observation is also made as the front plane is moved backward along the x-axis by about 40 μm. On further moving the plane backward along the x-axis by about another 40 μm, the bottom part of #2 pore channel is observed to be absent. The top part of #2 pore channel is observed to be connected to #1 pore channel (note pore branching as

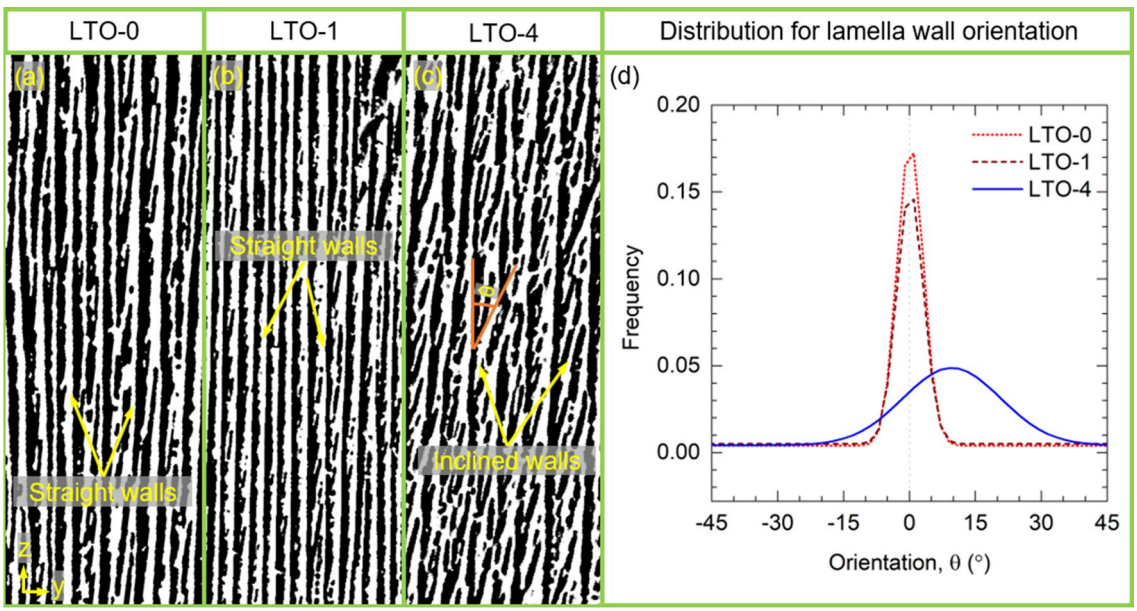

Figure 7: Binarized XCT 2D images of (a) LTO-0, (b) LTO-1, and (c) LTO-4 of y–z plane in the steady-state region. (d) Orientation distribution of lamella walls with respect to z-direction.

© The Author(s), under exclusive licence to The Materials Research Society 2021

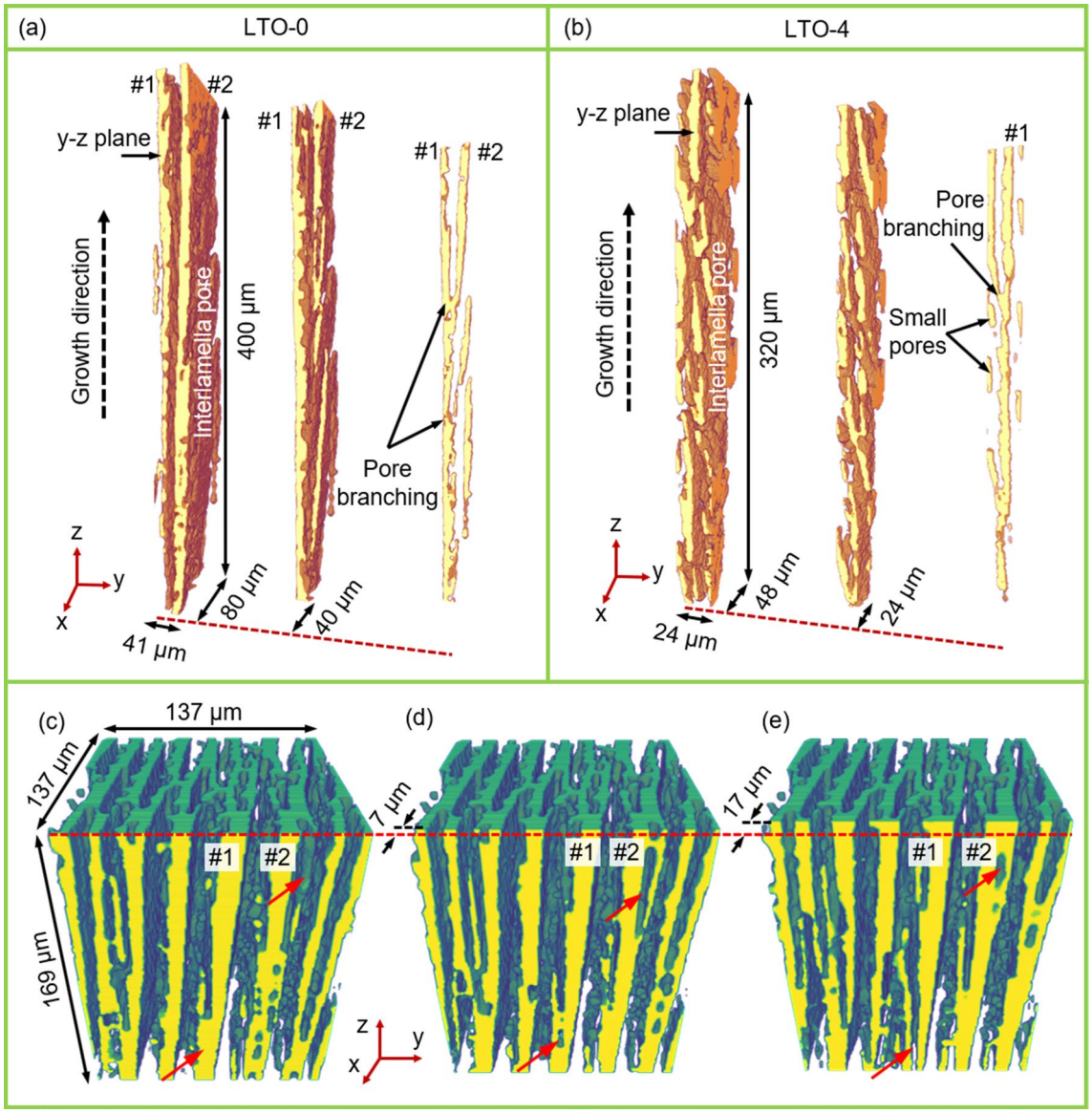

Figure 8: XCT images of individual pore channels in LTO-0 (a) and LTO-4 (b) over a distance of 400 µm, aligned along the *z*-axis. The front *y*–*z* plane is colored in yellow for better visualization, and the regions shown both in yellow and orange colors represent pores. For each material, the *y*–*z* plane is moved backward along the *x*-direction to reveal more details of the differences in the pore path characteristics in these materials. The connectivity between small and large pores is illustrated through several XCT images. (c) a 3D volume rendering for LTO-0. In (d) and (e), the *y*–*z* plane (front plane, colored in yellow for better visualization) is moved backward along the *x*-axis by 7 µm and 17 µm, respectively. The front plane is moved backward by small distances to reveal whether the pores observed within the ceramic walls are isolated (i.e., closed-pore) or connected to larger pore channels.

indicated in the image). Overall, in LTO-0, pore paths over 400 mm distance are relatively straight and continuous. On the other hand, pore channels in LTO-4 exhibit a considerably tortuous path with a high level of pore branching. As the front plane is moved backward along the *x*-axis by different distances, the tortuosity of the pore path becomes more obvious. In LTO-4, no single pore channel could be identified that is relatively straight along the growth direction. However, pore continuity along the growth direction is preserved in LTO-4 and hence directional porosity.

In the reconstructed 3D images, it also appears that pores are present within ceramic walls, as indicated in Fig. 6d. Dimensions of these pores are several micrometers, and they are not the ultrafine intralamellar pores (< 1 µm) present between LTO grains. Although it appears, not necessarily these pores are intralamellar type (i.e., completely enclosed within the walls and resulting in closed-cell pores) but are connected to larger interlamellar pore channels (directional pores). The connectivity between small and large pores is illustrated in Fig. 8c–e through several 3D images. Figure 8c shows a 3D volume rendering for

© The Author(s), under exclusive licence to The Materials Research Society 2021

LTO-0. In Fig. 8d and e, the y–z plane (front plane) is moved backward along the x-axis by 7 μm and 17 μm, respectively. Here, the front plane is moved backward by small distances to reveal whether the pores observed within the ceramic walls are isolated (i.e., closed-pore) or connected to larger pore channels. Two of the ceramic walls are numbered, #1 and #2. The red arrows on these walls point to the locations where observations are made on the appearance and disappearance of the pores. In Fig. 8c, no pore is observed in wall #1 at the specified location. However, as the front plane is moved backward by 7 μm, a small pore appears on wall #1 (Fig. 8d). Further moving the plane backward by 17 μm (Fig. 8e), it can be seen that a larger macropore (interlamellar pore) has appeared. A similar observation is made for wall #2 but in reverse order. In Fig. 8c, the red arrow on wall #2 shows a large macropore (interlamellar pore). As the plane is moved backward, it can be seen that the same macropore extended into the wall and appears as a small pore embedded within the wall. Similar observations were also made for LTO-1 and LTO-4 (not shown here). Therefore, on any vertical cross-section, pores observed within the ceramic walls are not isolated but connected to large interlamellar pores. The implication is significant since open-cell pore characteristic of ice-templated materials is well preserved, and all the pores could be accessible by a fluid. The apparent presence of small pores within the ceramic walls is attributed to the surface features of primary ice dendrites developed during the unidirectional freezing process.

Similar to the transition region, significant microstructural differences are also observed in the steady-state region, particularly between LTO-0 and LTO-4 materials. Both 2D and 3D images revealed that morphology is highly lamellar in LTO-0 but turned dendritic in LTO-4. Therefore, growth characteristics and morphology of ice crystals in the transition region are observed to be strongly correlated with the microstructure development in the steady-state region. The addition of 1 wt% sucrose caused a significant difference in the growth characteristics of ice crystals in the transition region. However, the microstructure of LTO-0 and LTO-1 is observed to be comparable in the steady-state region. On the other hand, by increasing sucrose content to 4 wt%, growth characteristics of ice crystals changed significantly both in the transition and steady-state region. A significant observation from reconstructed 3D images is that in LTO-4, in the steady-state region, primary ice crystals experienced significant tip splitting. The resulting secondary ice crystals grew into primary dendrites, and continuous meandering of ice crystals made the pore path highly tortuous. While 3D characterization of microstructure of materials at intermediate sucrose content is beyond the scope of this work, the current results strongly suggest that by using sucrose additive with varying content, microstructure and morphology in the transition region can be tuned and thereby microstructure in the steady-state region in ice-templated materials.

Pore tortuosity factor

Pore tortuosity differences in ice-templated sintered LTO materials is characterized by estimating pore tortuosity factor, τ, along directions parallel and perpendicular to growth direction (z-direction). Figure 9 shows 2D maps of normalized flux density projections on the x–y and x–z planes for LTO-0 (a), LTO-1 (e), and LTO-4 (i), resulting from tortuosity simulations. Local fluxes were summed through the volume and normalized in order to visualize flux density variation in 2D. On the x–z plane, diffusion direction is along the z-direction (growth direction of ice crystals) and the relevant directional tortuosity factor is τ_z. On the x–y plane, diffusion is simulated for both the x-direction and y-direction and the relevant directional tortuosity factors are τ_x and τ_y, respectively. Diffusion is simulated over the X-ray tomography data of volume $540 \times 540 \times 790$ μm^3. In each direction, to estimate τ, a concentration gradient is applied between the opposite faces. In the flux density maps, mass transport increases from dark to bright regions.

In LTO-0, τ_z (1.21) is lower than τ_x (2.44) and significantly lower than τ_y (55.4), which is because of the alignment of the pore channels along the z-direction, making this a preferred direction for mass transport. The unusually significant difference between τ_x and τ_y requires attention since this difference should not be taken as an indication of anisotropy on the x–y plane. In LTO-0, on the x–y plane within 540 μm × 540 μm area, only a few randomly oriented domains are present, with a large size domain occupying the majority of the area and thus the majority of the volume, giving an apparent pore directionality along the x-direction within this volume. Thus, the drastic difference in τ_x and τ_y simply arises from the size limit in the reconstructed volume over which diffusion simulation was performed. However, in the sintered sample with 13 mm diameter, numerous randomly oriented domains are present on the x–y plane and no pore directionality is expected on this plane over a larger area.

Simulation results for LTO-1 are comparable to that of LTO-0, particularly τ_z values. τ_z (1.16) is also observed to be lower than τ_x (7.29) and τ_y (5.01), again because of the alignment of the pore channels along the z-direction. In contrast to LTO-0, τ_x and τ_y values are comparable in LTO-1, which is because several randomly oriented domains are present on the x–y plane even within 540 μm × 540 μm area. In LTO-4, τ_z (1.52) is also observed to be significantly lower than τ_x (12.22) and τ_y (7.26). τ_x and τ_y values are comparable because of the presence of several randomly oriented domains on the x–y plane (540 μm × 540 μm). Both τ_x and τ_y values are relatively higher in LTO-4 because of the presence of numerous domains, enhancing tortuosity along the x- and y-directions. Figure 9 reveals that τ increased from LTO-0 to LTO-4. However, along the z-direction, the direction of interest for mass transport applications, increase in τ is relatively moderate. The estimated τ values of ice-templated LTO materials

© The Author(s), under exclusive licence to The Materials Research Society 2021

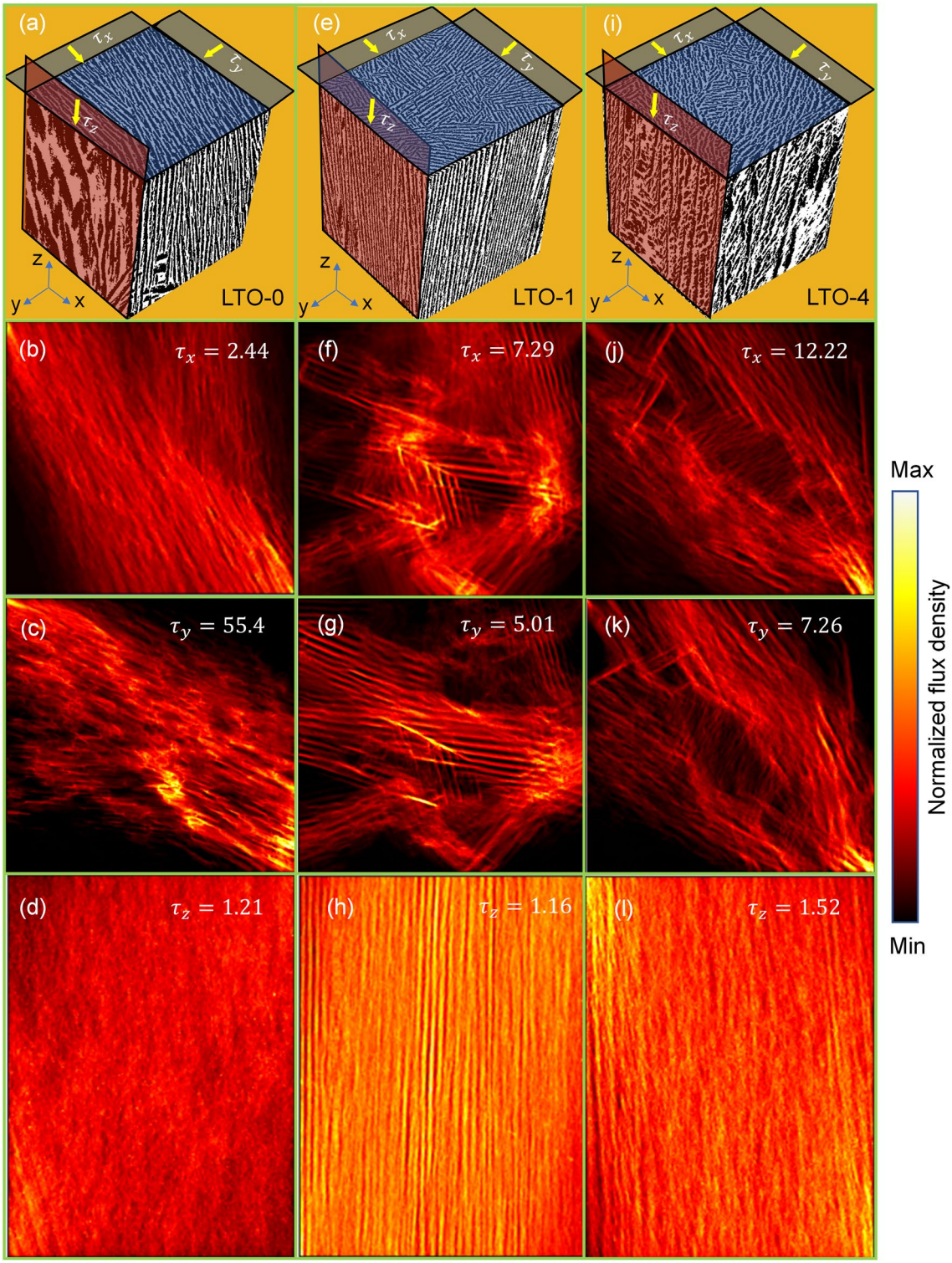

Figure 9: 2D maps of normalized flux density projections on the *x*–*y* and *x*–*z* planes for LTO-0 (a), LTO-1 (e), and LTO-4 (i), resulting from tortuosity simulations. On the *x*–*z* plane, diffusion direction is along the *z*-direction (also the growth direction of ice crystals) and the relevant directional tortuosity factor is τ_z. On the *x*–*y* plane, diffusion is simulated for both the *x*-direction and *y*-direction and the relevant directional tortuosity factors are τ_x and τ_y, respectively.

© The Author(s), under exclusive licence to The Materials Research Society 2021

are found to be comparable to the τ values reported for the other ice-templated ceramic materials [36, 55].

Conclusions

Significant insights into the influence of sucrose on morphology, orientation, and growth characteristics of ice crystals in both regions are provided from in-depth 2D and 3D microstructure characterizations of sintered materials. Based on the microstructural differences in the transition region and steady-state region between LTO-0 (fabricated without sucrose) and LTO-4 (fabricated with 4 wt% sucrose), the following conclusions are made:

1. Microstructure characterization from SEM images of x–y planes at different heights along the z-direction suggested that MS interface instability occurred in both materials, as the growth front changed from planar to cellular to lamellar/dendritic morphology.
2. 2D characterizations revealed that in LTO-0, lamella walls grew with random orientations up to a significant height in the transition region before achieving the preferred alignment. This behavior was rationalized based on the concept of r-crystal and z-crystal domains and their thermal conductivity differences.
3. 2D characterizations further revealed that characteristic ice-templated microstructure fully developed within a shorter distance along z-direction in LTO-4 (thus wall alignment) and hence the shorter length of transition region than in LTO-0. Microstructure development in this zone in LTO-4 was remarkably different than in LTO-0. Sucrose strongly influenced the morphology, orientation, and growth characteristics of ice crystals in the transition region. The differences were rationalized based on constitutional supercooling and interface instability.
4. Pore morphology changed from highly lamellar in LTO-0 to dendritic in LTO-4, quantified by estimating a dimensionless morphological parameter "m".
5. 3D characterization revealed relatively straight ceramic walls and pore channels in the steady-state region in LTO-0. Tip splitting of primary ice dendrites and growth of secondary ice dendrites were limited.
6. In LTO-4, side branching of walls increased and hence interlamellar connectivity. 3D images revealed that increased branching of walls originated from increased branching of primary ice dendrites. Primary ice dendrites exhibited greatly enhanced tip splitting, and a majority of the secondary dendrites grew into neighboring primary dendrites. The significant differences in the pore path between LTO-0 and LTO-4 were further revealed through 3D images of a few individual pore channels.
7. Using TauFactor application in MATLAB and reconstructed 3D images, the tortuosity factor was estimated using diffusion simulations. Pore tortuosity increased from LTO-0 to LTO-4. However, along the z-direction, the direction of interest, increase in tortuosity was moderate.

Methods

Preparation of aqueous LTO suspensions

Ice-templated LTO materials were fabricated from NANOMYTE® BE-10 LTO powder (NEI Corporation, Somerset, NJ, purity > 98%). A two-step sieving process was developed to break the large agglomerates present in the as-received powder, and the details can be found elsewhere [23]. Materials were fabricated from 20 vol% aqueous suspensions of LTO of three different compositions. Suspensions of one composition were without sucrose, and the resultant materials are referred to as LTO-0. For the other two compositions, suspensions contained 1 and 4 wt% sucrose (with respect to the water content in suspension), and the resultant materials are referred to as LTO-1 and LTO-4, respectively.

LTO-0 suspensions were prepared by mixing LTO powder with deionized (DI) water containing cationic dispersant (1-hexadecyl)trimethylammonium bromide (CTAB, Alfa Aesar, Haverhill, MA) in the concentration of 0.02 g/cm^3 with respect to DI water volume. An antifoaming agent SURFYNOL®104P G 50 (Evonik Industries), in the proportion of 0.3 wt% of LTO powder, was also used. LTO-1 and LTO-4 suspensions were prepared without CTAB and antifoaming agent. Commercially available sucrose (Saccharose, Sigma-Aldrich) was dissolved in DI water, and then LTO powder was added. Suspensions were milled using zirconia (ZrO_2) spheres (5 mm diameter) with 1:4 mass ratio to LTO powder. Milling was first performed for 1 h at 30 rpm. Next, binder solution was added (4 wt% of LTO powder), and the suspension was milled for another one hour. The binder solution was prepared by dissolving poly(2-ethyl-2-oxazoline) (Alfa Aesar) in DI water (2.5 times of binder mass). From suspensions, ZrO_2 spheres were separated using a 325 mesh (45 μm).

pH of all the suspensions, measured using pH meter (HI2255, Hanna Instruments), was close to 11. The suspensions prepared with sucrose appeared relatively viscous compared to the suspensions prepared without sucrose. Viscosity of LTO-0, LTO-1 and LTO-4 suspensions were measured using Anton Paar MCR302 rheometer at room temperature. During the measurement, shear rate was varied from 0.1 to 5 s^{-1}. For each composition, three measurements were conducted for reproducibility.

© The Author(s), under exclusive licence to The Materials Research Society 2021

Fabrication of ice-templated sintered LTO materials

Ice-templating was performed using a custom-made device [8, 56]. In this setup, a Teflon tube (inner diameter 16 mm, height 25 mm, wall thickness 5 mm) is placed on a thin copper (Cu) plate ("Cold-finger") and filled with ceramic suspension. Next, the entire assembly is inserted inside liquid nitrogen (N_2) Dewar but placed above the liquid level. As the temperature of the Cu plate reaches below 0 °C, ice crystals nucleate at the bottom of suspension in contact with Cold-finger and grow upward. All the materials were fabricated at 1 mm gap between the Cold-finger and liquid N_2. From each batch of LTO suspension, four samples were ice-templated with average FFV of 34.04 ± 1.8 μm/s, 31.7 ± 1.7 μm/s, and 33.1 ± 1.2 μm/s for LTO-0, LTO-1, and LTO-4, respectively. Frozen samples were freeze-dried (2.5 L, Labconco, Kansas City, MI) for 96 h at a pressure of 0.014 mbar and temperature of – 50 °C. Next, samples were sintered at 950 °C for 2 h in an air atmosphere inside a tube furnace (NBD, T-1700-60IT). Details of the sintering cycle can be found elsewhere [23]. Sintered LTO cylinder samples were approximately 13 mm in diameter and 7 mm in height. Porosity values (estimated from measurements of mass and dimensions of sintered samples) of LTO-0, LTO-1 and LTO-4 materials were 63.6 ± 0.4, 59.6 ± 0.3 and 59.3 ± 0.1 vol%, respectively.

Characterization of microstructure in transition region and steady-state region

A desktop SEM (Phenom Pure, Thermo Fisher Scientific) was used to investigate microstructure in the transition region (Fig. 10a). For each composition, one sintered sample was vertically sectioned into two specimens. In one specimen, the microstructure on the *x*–*z* plane along the *z*-direction was studied, where *z*-direction is the direction of the temperature gradient and the dominant growth direction. The material was removed from the bottom of the other specimen in small increments along *z*-direction using a 1200 grit SiC paper, and microstructure on *x*–*y* planes was evaluated.

XCT was performed to study microstructure in the steady-state region. For each composition, a sintered sample was first infiltrated with epoxy. Using a diamond saw, from each infiltrated sample, a disk of 3 mm thickness from 2 mm height from the bottom along *z*-direction was removed (Fig. 10b). Next, a small specimen of dimensions 1.5 mm × 1.5 mm × 3 mm was extracted and used for XCT. The extracted specimens were scanned using a Zeiss Xradia 510 Versa 3D XRM (Carl Zeiss X-ray Microscopy, Pleasanton, CA, USA) with 80 kV X-ray source, 80 μA target current, and 15 s exposure time. Tomography data was measured from the mid-section of each specimen. X-ray radiographs were reconstructed using XRM

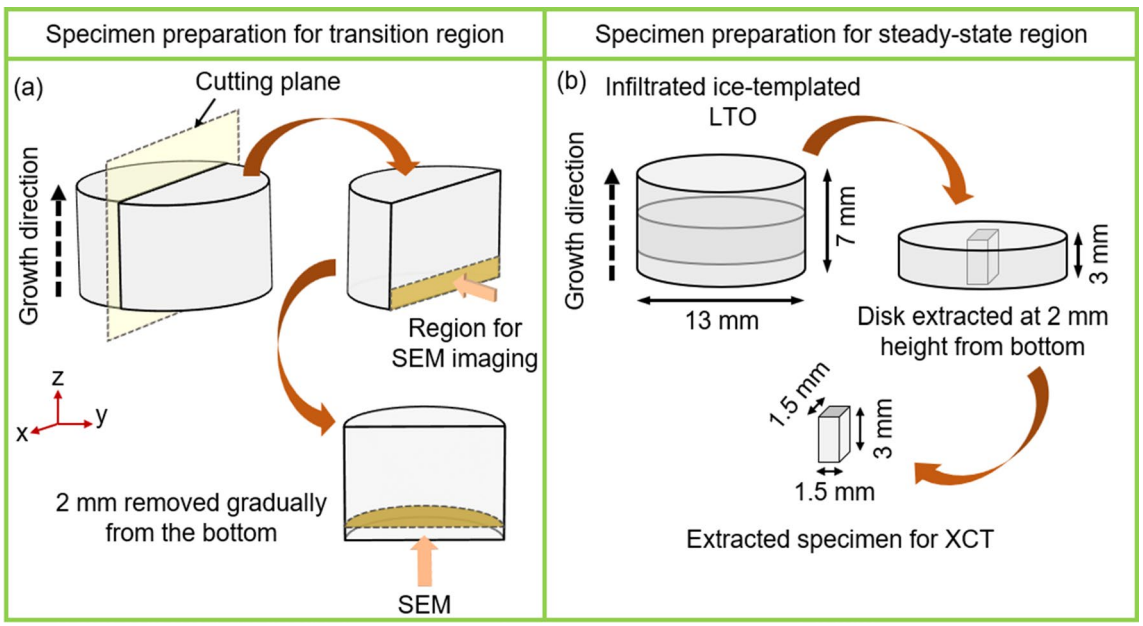

Figure 10: Schematics of the steps for specimen preparation for microstructure investigation in the (a) transition region and (b) steady-state region of ice-templated materials. (a) Ice-templated sintered LTO sample cut vertically into two halves and microstructure in the transition region was analyzed using SEM. In one specimen, bottom region (*x*–*z* plane, highlighted in yellow) was investigated to study microstructure evolution in the transition region along *z*-direction. For the other specimen, material up to 2 mm height along *z*-direction from was gradually removed and *x*–*y* plane at different heights was investigated to study microstructure evolution in the transition region along *z*-direction. (b) From epoxy infiltrated ice-templated sintered LTO sample, first, a disk of 3 mm thickness from 2 mm height from the bottom along *z*-direction was removed. Next, a specimen of dimensions 1.5 mm × 1.5 mm × 3 mm was extracted and used to study microstructure in the steady-state region using XCT. Tomography data was measured from the mid-section of each specimen.

© The Author(s), under exclusive licence to The Materials Research Society 2021

Reconstructor software. The 3D structure was constructed from 987 2D X-ray radiographs (2D images along the z-direction) with an image resolution of 1008×984 pixels with a pixel size of 800 nm.

3D visualization of microstructure in steady-state region

Details of the binarization of XCT 2D images are provided in the Supplementary Materials. From binarized 2D images, 3D images were reconstructed to visualize microstructure in the steady-state region, which was performed employing Dragonfly 2020.1 software (Object Research Systems, Montreal). Using Dragonfly, 3D volume renderings of ceramic walls and pores were created.

Characterization of pore tortuosity

Using an open-source TauFactor application in MATLAB and reconstructed binarized nano-CT 3D images, the tortuosity factor (τ, a single scalar value) was estimated by performing diffusion simulations [35–37]. τ quantifies the degree of transport reduction caused by the convolutions of flow paths, such as pores. Thus, from the microstructural image data, TauFactor determines the reduction in diffusive mass transport caused by the geometrical convolutions of a heterogeneous media [32–34]. TauFactor performs diffusion simulation on 3D segmented image data and compares steady-state diffusive flow through a pore network relative to that through a fully dense control volume of the same size, diffusivity, and potential difference. The effect of the heterogeneous media such as pores on the reduction in diffusive transport is captured in term of τ as [35–37]:

$$\tau = \frac{D_0 \varepsilon}{D_{\text{eff}}}. \tag{5}$$

D_0 is the intrinsic diffusivity of the conductive phase, and D_{eff} is the effective diffusivity through a porous volume where the second phase is insulating. ε represents the volume fraction of the conductive phase (pores).

Acknowledgments

The authors thank the US National Science Foundation (NSF) for the support of this work, via Grant CMMI-1825338. DG acknowledges a Supplemental Award through NSF DCL 20-027, "Data Science Activities for the Civil, Mechanical and Manufacturing Innovation Communities", for the partial support of this work. The authors acknowledge Professor Jacob L. Jones (Department of Materials Science and Engineering, North Carolina State University) for providing access to Zeiss Xradia 510 Versa 3D XRM in Analytical Instrumentation Facility (AIF) at NC State for X-ray computed tomography. The authors also acknowledge the help of Dr. Anton Jansson and Dr. Sanaz Koohfar (AIF Postdocs) for XCT measurements. The authors acknowledge the help of Mr. Mazen Mezher (PhD student) and Professor Venkat Maruthamuthu (Old Dominion University) for viscosity measurements.

Declarations

Conflict of interest On behalf of all authors, the corresponding author states that there is no conflict of interest.

Supplementary Information

The online version contains supplementary material available at https://doi.org/10.1557/s43578-021-00367-3.

References

1. K.L. Scotti, D.C. Dunand, Freeze casting—a review of processing, microstructure and properties via the open data repository, FreezeCasting.net. Prog. Mater. Sci. **94**, 243 (2018)
2. I. Nelson, S.E. Naleway, Intrinsic and extrinsic control of freeze casting. J. Mater. Res. Technol. **8**, 2372 (2019)
3. D. Ghosh, H. Kang, M. Banda, V. Kamaha, Influence of anisotropic grains (platelets) on the microstructure and uniaxial compressive response of ice-templated sintered alumina scaffolds. Acta Mater. **125**, 1 (2017)
4. M.M. Porter, R. Imperio, M. Wen, M.A. Meyers, J. McKittrick, Bioinspired scaffolds with varying pore architectures and mechanical properties. Adv. Funct. Mater. **24**, 1978 (2014)
5. M. Banda, D. Ghosh, Effects of porosity and strain rate on the uniaxial compressive response of ice-templated sintered macroporous alumina. Acta Mater. **149**, 179 (2018)
6. S. Akurati, D. Ghosh, M. Banda, D. Terrones, Direct observation of failure in ice-templated ceramics under dynamic and quasistatic compressive loading conditions. J. Dyn. Behav. Mater. **5**, 463 (2019)
7. S. Akurati, J. Marin, B. Gundrati, D. Ghosh, Assessing the role of loading direction on the uniaxial compressive response of multilayered ice-templated alumina–epoxy composites. Materialia **14**, 100895 (2020)
8. D. Ghosh, N. Dhavale, M. Banda, H. Kang, A comparison of microstructure and uniaxial compressive response of ice-templated alumina scaffolds fabricated from two different particle sizes. Ceram. Int. **42**, 16138 (2016)
9. D. Ghosh, M. Banda, N. Dhavale, H. Kang, Platelet-induced stiffening and strengthening of ice-templated Al_2O_3 scaffolds. Scr. Mater. **125**, 29 (2016)

© The Author(s), under exclusive licence to The Materials Research Society 2021

10. S. Akurati, D. Terrones, D. Ghosh, Role of microstructure on impact response and damage morphology of ice-templated porous ceramics. J. Dyn. Behav. Mater. **7**, 2 (2021)
11. C.M. Pekor, P. Kisa, I. Nettleship, Effect of polyethylene glycol on the microstructure of freeze-cast alumina. J. Am. Ceram. Soc. **91**, 3185 (2008)
12. C. Pekor, B. Groth, I. Nettleship, The effect of polyvinyl alcohol on the microstructure and permeability of freeze-cast alumina. J. Am. Ceram. Soc. **93**, 115 (2010)
13. S. Deville, Freeze-casting of porous ceramics: a review of current achievements and issues. Adv. Eng. Mater. **10**, 155 (2008)
14. B. Delattre, H. Bai, R.O. Ritchie, J. De Coninck, A.P. Tomsia, Unidirectional freezing of ceramic suspensions: in situ X-ray investigation of the effects of additives. Appl. Mater. Interfaces **6**, 159 (2014)
15. E. Munch, E. Saiz, A.P. Tomsia, S. Deville, Architectural control of freeze-cast ceramics through additives and templating. J. Am. Ceram. Soc. **92**, 534 (2009)
16. I. Nelson, L. Gardner, K. Carlson, S.E. Naleway, Freeze casting of iron oxide subject to a tri-axial nested Helmholtz-coils driven uniform magnetic field for tailored porous scaffolds. Acta Mater. **173**, 106 (2019)
17. M.B. Frank, S.H. Siu, K. Karandikar, C.H. Liu, S.E. Naleway, M.M. Porter, O.A. Graeve, J. McKittrick, Synergistic structures from magnetic freeze casting with surface magnetized alumina particles and platelets. J. Mech. Behav. Biomed. Mater. **76**, 153 (2017)
18. T.A. Ogden, M. Prisbrey, I. Nelson, B. Raeymaekers, S.E. Naleway, Ultrasound freeze casting: fabricating bioinspired porous scaffolds through combining freeze casting and ultrasound directed self-assembly. Mater. Des. **164**, 107561 (2019)
19. M. Mroz, J.L. Rosenberg, C. Acevedo, J.J. Kruzic, B. Raeymaekers, S.E. Naleway, Ultrasound freeze-casting of a biomimetic layered microstructure in epoxy–ceramic composite materials to increase strength and hardness. Materialia **12**, 100754 (2020)
20. Y. Tang, S. Qiu, Q. Miao, C. Wu, Fabrication of lamellar porous alumina with axisymmetric structure by directional solidification with applied electric and magnetic fields. J. Eur. Ceram. Soc. **36**, 1233 (2016)
21. Y.F. Tang, K. Zhao, J.Q. Wei, Y.S. Qin, Fabrication of aligned lamellar porous alumina using directional solidification of aqueous slurries with an applied electrostatic field. J. Eur. Ceram. Soc. **30**, 1963 (2010)
22. Y. Zhang, L. Hu, J. Han, Preparation of a dense/porous bilayered ceramic by applying an electric field during freeze casting. J. Am. Ceram. Soc. **92**, 1874 (2009)
23. R. Parai, T. Walters, J. Marin, S. Pagola, G.M. Koenig Jr., D. Ghosh, Strength enhancement in ice-templated lithium titanate $Li_4Ti_5O_{12}$ materials using sucrose. Materialia **14**, 100901 (2020)
24. Z. Nie, S. Ong, D.S. Hussey, J.M. LaManna, D.L. Jacobson, G.M. Koenig Jr., Probing transport limitations in thick sintered battery electrodes with neutron imaging. Mol. Syst. Des. Eng. **5**, 245 (2020)
25. Z. Qi, G.M. Koenig Jr., Electrochemical evaluation of suspensions of lithium-ion battery active materials as an indicator of rate capability. J. Electrochem. Soc. **164**, A151 (2017)
26. S. Deville, E. Saiz, A.P. Tomsia, Ice-templated porous alumina structures. Acta Mater. **55**, 1965 (2007)
27. S. Deville, E. Maire, A. Lasalle, A. Bogner, C. Gauthier, J. Leloup, C. Guizard, In situ X-ray radiography and tomography observations of the solidification of aqueous alumina particle suspensions—Part I: initial instants. J. Am. Ceram. Soc. **92**, 2489 (2009)
28. T. Waschkies, R. Oberacker, M.J. Hoffmann, Investigation of structure formation during freeze-casting from very slow to very fast solidification velocities. Acta Mater. **59**, 5135 (2011)
29. S. Deville, E. Maire, A. Lasalle, A. Bogner, C. Gauthier, J. Leloup, C. Guizard, In situ X-ray radiography and tomography observations of the solidification of aqueous alumina particles suspensions—Part II: steady state. J. Am. Ceram. Soc. **92**, 2497 (2009)
30. E. Maire, X-ray tomography applied to the characterization of highly porous materials. Annu. Rev. Mater. Res. **42**, 163 (2012)
31. X. Ou, X. Zhang, T. Lowe, R. Blanc, M.N. Rad, Y. Wang, N. Batail, C. Pham, N. Shokri, A.A. Garforth, P.J. Withers, X. Fan, X-ray micro computed tomography characterization of cellular SiC foams for their applications in chemical engineering. Mater. Charact. **123**, 20 (2017)
32. B. Ghanbarian, A.G. Hunt, R.P. Ewing, M. Sahimi, Tortuosity in porous media: a critical review. Soil Sci. Soc. Am. J. **77**, 1461 (2013)
33. B. Tjaden, D.J.L. Brett, P.R. Shearing, Tortuosity in electrochemical devices: a review of calculation approaches. Int. Mater. Rev. **63**, 47 (2018)
34. F.L.E. Usseglio-Viretta, D.P. Finegan, A. Colclasure, T.M.M. Heenan, D. Abraham, P. Shearing, K. Smith, Quantitative relationships between pore tortuosity, pore topology, and solid particle morphology using a novel discrete particle size algorithm. J. Electrochem. Soc. **167**, 100513 (2020)
35. S.J. Cooper, A. Bertei, P.R. Shearing, J.A. Kilner, N.P. Brandon, TauFactor: an open-source application for calculating tortuosity factors from tomographic data. SoftwareX **5**, 203 (2016)
36. C. Huang, M. Dontigny, K. Zaghib, P.S. Grant, Low-tortuosity and graded lithium ion battery cathodes by ice templating. J. Mater. Chem. A **7**, 21421 (2019)
37. S.J. Cooper, Quantifying the transport properties of solid oxide fuel cell electrodes, PhD Thesis, Imperial College, London, 2015
38. Z. Nie, P. McCormack, H.Z. Bilheux, J.C. Bilheux, P. Robinson, J. Nanda, G.M. Koenig Jr., Probing lithiation and delithiation of

© The Author(s), under exclusive licence to The Materials Research Society 2021

thick sintered lithium-ion battery electrodes with neutron imaging. J. Power Sources **419**, 127 (2019)
39. W.W. Mullins, R.F. Sekerka, Stability of a planar interface during solidification of dilute binary alloy. J. Appl. Phys. **35**, 444 (1964)
40. D. Mandal, D. Sathiyamoorthy, M. Vinjamur, Experimental measurement of effective thermal conductivity of packed lithium-titanate pebble bed. Fusion Eng. Des. **87**, 67 (2012)
41. M.E. Glicksman, *Principles of Solidification* (Springer, New York, 2011)
42. C.M. Pekor, The effect of water-soluble polymers on the microstructure and properties of freeze-cast alumina ceramics, PhD Dissertation, University of Pittsburgh, 2010
43. W. Kurz, D.J. Fisher, *Fundamentals of Solidification—4th Revised Edition* (Trans Tech Publications LTD, Bach, 1998)
44. W.A. Tiller, K.A. Jackson, J.W. Rutter, B. Chalmers, The redistribution of solute atoms during the solidification of metals. Acta Metall. **1**, 428 (1953)
45. J. You, L. Wang, Z. Wang, J. Li, J. Wang, X. Lin, W. Huang, Interfacial undercooling in solidification of colloidal suspensions: analyses with quantitative measurements. Sci. Rep. **6**, 28434 (2016)
46. C. Pekor, I. Nettleship, The effect of the molecular weight of polyethylene glycol on the microstructure of freeze-cast alumina. Ceram. Int. **40**, 9171 (2014)
47. J.D. Harrison, W.A. Tiller, Ice interface morphology and texture developed during freezing. J. Appl. Phys. **34**, 3349 (1963)
48. S. Sabat, S. Sikder, S.K. Behera, A. Paul, Effect of freezing velocity and platelet size on structural parameters and morphology of freeze-cast porous alumina scaffolds. Ceram. Int. **47**, 16661 (2021)
49. R. Okaji, K. Taki, S. Nagamine, M. Ohshima, Preparation of porous honeycomb monolith from UV-curable monomer/dioxane solution via unidirectional freezing and UV irradiation. J. Appl. Polym. Sci. **125**, 2874 (2012)
50. A. Lasalle, C. Guizard, J. Leloup, S. Deville, E. Maire, A. Bogner, C. Gauthier, J. Adrien, L. Courtois, Ice-templating of alumina suspensions: effect of supercooling and crystal growth during the initial freezing regime. J. Am. Ceram. Soc. **95**, 799 (2012)
51. R. Liu, J. Yuan, C. Wang, A novel way to fabricate tubular porous mullite membrane supports by TBA-based freezing casting method. J. Eur. Ceram. Soc. **33**, 3249 (2013)
52. V. Naglieri, H.A. Bale, B. Gludovatz, A.P. Tomsia, R.O. Ritchie, On the development of ice-templated silicon carbide scaffolds for nature-inspired structural materials. Acta Mater. **61**, 6948 (2013)
53. S. Roy, B. Butz, A. Wanner, Damage evolution and domain-level anisotropy in metal/ceramic composites exhibiting lamellar microstructures. Acta Mater. **58**, 2300 (2010)
54. S. Akurati, A. Jansson, J.L. Jones, D. Ghosh, Deformation mechanisms in ice-templated alumina–epoxy composites for the different directions of uniaxial compressive loading. Materialia **16**, 101054 (2021)
55. S.M. Miller, X. Xiao, K.T. Faber, Freeze-cast alumina pore networks: effects of freezing conditions and dispersion medium. J. Eur. Ceram. Soc. **35**, 3595 (2015)
56. N. Dhavale, A comparison of microstructure and uniaxial compressive response of ice-templated porous alumina scaffolds fabricated from two different particle sizes, Master's Thesis, Old Dominion University, 2016

© The Author(s), under exclusive licence to The Materials Research Society 2021